Connectivity between primary and secondary subglacial drainage systems beneath a land-terminating outlet glacier of the Greenland Ice Sheet

R. Ing[1,2], E. Bagshaw[2], J. Hawkins[3], M. Peacey[4, 2], S. Doyle[4, 5], S. Livingstone[5], M. Prior-Jones[3], S. Thorpe[5], A. Moffatt[5], A. Sole[5], G. Bianchi[3], A. Booth[6], S. Buzzard[7], T. Chudley[8,1], C. Clason[8], L. Craw[3], L. Edwards[9], F. Gimbert[10], A. Hepburn[4], A. Jones[11], T. Le Bris[10], S. Mann[3], A. Michel[10], N. Ross[12], R. Storrar[11], R. Veness[11] and T. Young[13]

[1]School of Geosciences, University of Edinburgh, Edinburgh, UK
[2]School of Geographical Sciences, University of Bristol, Bristol, UK
[3]School of Earth & Environmental Sciences, Cardiff University, Cardiff, UK
[4]Centre for Glaciology, Department of Geography and Earth Sciences, Aberystwyth University, Aberystwyth, SY23 3DB, UK
[5]School of Geography and Planning, University of Sheffield, Sheffield, S3 7ND
[6]School of Earth, Environment and Sustainability, University of Leeds, Leeds, UK
[7]Department of Geography and Environmental Sciences, Northumbria University, Newcastle upon Tyne, United Kingdom
[8]Department of Geography, Durham University, Durham, UK
[9]School of Biological & Environmental Sciences, Liverpool John Moores University, Liverpool L3 3AF, UK
[10]Université Grenoble Alps UGA, Institute for Geoscience and Environment IGE, CNRS, Grenoble, France
[11]Geography, Environment and Planning, Sheffield Hallam University, Howard Street, Sheffield, S1 1WB
[12]School of Geography, Politics and Sociology, Newcastle University, Newcastle upon Tyne, UK
[13]School of Geography and Sustainable Development, University of St Andrews, St Andrews, UK

Corresponding author: Ryan Ing (ryan.ing@ed.ac.uk)
https://orcid.org/0000-0001-9767-3209

Connectivity between primary and secondary subglacial drainage systems beneath a land-terminating outlet glacier of the Greenland Ice Sheet

R. Ing[1,2], E. Bagshaw[2], J. Hawkins[3], M. Peacey[4, 2], S. Doyle[4, 5], S. Livingstone[5], M. Prior-Jones[3], S. Thorpe[5], A. Moffatt[5], A. Sole[5], G. Bianchi[3], A. Booth[6], S. Buzzard[7], T. Chudley[8,1], C. Clason[8], L. Craw[3], L. Edwards[9], F. Gimbert[10], A. Hepburn[4], A. Jones[11], T. Le Bris[10], S. Mann[3], A. Michel[10], N. Ross[12], R. Storrar[11], R. Veness[11] and T. Young[13]

[1]School of Geosciences, University of Edinburgh, Edinburgh, UK
[2]School of Geographical Sciences, University of Bristol, Bristol, UK
[3]School of Earth & Environmental Sciences, Cardiff University, Cardiff, UK
[4]Centre for Glaciology, Department of Geography and Earth Sciences, Aberystwyth University, Aberystwyth, SY23 3DB, UK
[5]School of Geography and Planning, University of Sheffield, Sheffield, S3 7ND
[6]School of Earth, Environment and Sustainability, University of Leeds, Leeds, UK
[7]Department of Geography and Environmental Sciences, Northumbria University, Newcastle upon Tyne, United Kingdom
[8]Department of Geography, Durham University, Durham, UK
[9]School of Biological & Environmental Sciences, Liverpool John Moores University, Liverpool L3 3AF, UK
[10]Université Grenoble Alps UGA, Institute for Geoscience and Environment IGE, CNRS, Grenoble, France
[11]Geography, Environment and Planning, Sheffield Hallam University, Howard Street, Sheffield, S1 1WB
[12]School of Geography, Politics and Sociology, Newcastle University, Newcastle upon Tyne, UK
[13]School of Geography and Sustainable Development, University of St Andrews, St Andrews, UK

Corresponding author: Ryan Ing (ryan.ing@ed.ac.uk)

Key Points:

- Hydraulic connectivity between primary and secondary subglacial drainage switches on hourly timescales over spatial scales of 100s of meters
- Large subglacial drainage axes, fed by upstream sources, dictate regional ice dynamics
- Wireless 'Cryoegg' sensors measure moulin electrical conductivity and hydraulic head and reveal long-term changes in drainage behavior

Abstract

The evolution and connectivity of subglacial drainage systems controls basal sliding and therefore modulates ice flow, yet direct observations of these systems remain limited. Here, we investigate hydraulic connectivity and its influence on ice motion at Isunnguata Sermia - a large land-terminating outlet glacier of the Greenland Ice Sheet. We use 'Cryoegg' wireless sensors to obtain moulin water pressure and electrical conductivity, in conjunction with passive seismics to measure glacio-hydraulic tremor and GNSS-derived measurements of ice motion. We identify rapid switching (<24 hours) of subglacial hydraulic connectivity between a large, primary subglacial drainage axis located in a deep trough, and subsidiary secondary subglacial channels. When surface melt inputs are high, the secondary channels fed by the instrumented moulins couple to the efficient primary subglacial drainage axis, exhibiting smoothed diurnal variability and synchronization with regional ice motion and seismic tremor. When melt inputs decrease, the secondary drainage system becomes isolated and responds sensitively to variations in local melt inputs, causing a reduction in hydraulic connectivity and an increase in local meltwater residence time. Regional ice motion appears completely controlled by the characteristics of the primary subglacial drainage axis and is insensitive to local inputs to secondary channels.

Plain Language Summary

Subglacial drainage systems transport meltwater beneath glaciers to downstream environments. Because the structure of the drainage system controls where water flows and hence how slippery parts of the ice bed may be, it influences ice motion, yet directly observing these systems is extremely difficult. We use sensors, including wireless "Cryoeggs", deployed into moulins, to measure water pressure and electrical conductivity variations as daily surface ice melt inputs fluctuate over the summer melt season. We combine these data with measurements of seismic tremor caused by flowing water and ice motion from GPS stations to explore the interactions between primary and secondary subglacial drainage systems. We find that variations in surface meltwater input cause the drainage system to rapidly switch between: (1) 'connected' states associated with flooding of the main drainage route during warm periods, which captures the local flow; and (2) 'disconnected' states associated with cooler periods, when the main drainage route becomes more restricted and the system fragments into smaller catchments that respond to local melt inputs. Ice motion is largely controlled by the fluctuating regional drainage system rather than the smaller local catchments.

1 Introduction

Surface meltwater in the ablation area of the Greenland Ice Sheet (GrIS) accesses the glacier bed through crevasses and moulins, and is then routed through the subglacial drainage system. Drainage configurations evolve between hydraulically inefficient, distributed components (e.g., linked cavities, thin films and Darcian flow through permeable sediments; Kamb, 1987; Clarke 1987) and efficient, channelized structures (Röthlisberger, 1972; Nye, 1976; Ng, 2000) in response to variations in meltwater inputs (Schoof, 2010). The variance in evolving hydraulic connectivity between these configurations determines the overall efficiency of the subglacial drainage system (Lefeuvre et al., 2015, Rada & Schoof, 2018), and controls subglacial water pressure and its transmission across the bed (Lefeuvre et al., 2018; Murray & Clarke, 1995;

Werder et al., 2013). Variations in subglacial water pressure modulate basal sliding and ice motion over spatial scales defined by longitudinal stress coupling lengths (Kamb, 1987; Iken and Bindschadler, 1986; Ryser at el., 2014). Measurements of meltwater hydraulic head in moulins or boreholes can thus act as a manometer of these hydrological changes (Hubbard et al. 1995; Andrews et al. 2014).

Direct measurements of subglacial pressure variations are therefore critical for improving our understanding of the evolution of the subglacial drainage, its influence on ice sheet dynamics (Andrews et al., 2014; Cowton et al., 2016), and for informing process-based models of subglacial hydrology (e.g., Flowers et al., 2003; Schoof 2010; Hewitt et al., 2013; Hoffman et al., 2011; Werder et al. 2013). Long-term measurements of water pressure from borehole arrays on mountain glaciers have revealed that subglacial drainage systems can undergo shifts in connectivity. As subglacial water flow declines and effective pressure in channels decreases, shifts in local hydraulic gradients can lead to the hydrological isolation of parts of the subglacial system, causing the drainage network to fragment into distinct, isolated subsystems (Rada and Schoof 2018; 2023) that respond independently to local meltwater inputs. Simultaneous measurement of electrical conductivity (EC) can enable proxy assessment of meltwater residence time (Brown et al., 1994), sediment availability (Collins, 1979), and meltwater origin (Gordon et al., 1998), providing further evidence of meltwater isolation.

On the GrIS, direct observations from boreholes have provided detailed records of basal water pressure and assessment of drainage configurations (e.g., Lüthi et al., 2002; Meierbachtol et al., 2013; Andrews et al. 2014; Wright et al., 2016; Doyle et al., 2018; 2022). These data are particularly powerful when used in tandem with surface measurements of ice motion across spatial scales sufficient that capture both regional and local subglacial processes (Andrews et al., 2014; Doyle et al., 2013; Mejia et al., 2022). GNSS-derived ice motion is a well-established method for inferring subglacial efficiency; increases in surface velocity typically relate to regional basal water pressure variations, while surface uplift can indicate hydraulic jacking (Iken et al., 1983; Iken and Bindschadler, 1986; van de Wal et al., 2008). Passive seismic observations provide a complementary perspective, where glacio-hydraulic tremor serves as a proxy for temporal variations in regional subglacial discharge, where increased turbulence in subglacial channels correlate with higher seismic power at specific frequencies (Bartholomaus et al., 2015; Gimbert et al., 2016; Mejia et al., 2022). However, our current understanding of GrIS subglacial drainage remains limited by the sparse and spatially restricted nature of direct observations, making it challenging to infer large-scale drainage connectivity and properties (Luthi, 2013), and the limited intersection between surface and sub-surface measurements of active drainage routes.

While boreholes offer stochastic access to the subglacial drainage system, often intercepting poorly connected cavities, moulins provide direct access to channelized drainage and the hydraulic response of subglacial channels to surface melt variability. Combining these data with surface dynamic observations (e.g., Andrews et al. 2014; Cowton et al., 2013; 2016; Mejia et al., 2021; 2022; Covington et al., 2020) can reveal hydrological behaviours often analogous to those observed in mountain glaciers, including seasonally evolving subglacial drainage that modulates ice sliding speeds (Andrews et al., 2014; Hoffman et al., 2011). Previous studies have typically

116 targeted moulins with large supraglacial inputs (~10^{-1} to 10 $m^3 s^{-1}$; e.g., Andrews et al., 2014;
117 Cowton et al., 2016), but the dynamics of smaller, local, secondary channels and their
118 connectivity to larger, primary subglacial drainage axes remain less well constrained. These
119 smaller channels likely deliver significant meltwater inputs to the primary drainage system, with
120 a periodicity that could modulate hydraulic response. We aim to explore the evolving hydraulic
121 connectivity of primary and secondary subglacial drainage systems beneath a land-terminating
122 outlet glacier of the GrIS through the deployment of novel wireless "Cryoegg" sensors and a
123 cabled piezometer, to measure water pressure and electrical conductivity (EC) in small moulins.
124 These observations occurred in tandem with high resolution GNSS-derived ice motion, passive
125 surface measurements of seismic tremor as a proxy for subglacial water discharge and
126 meteorological measurements of surface melt, to develop a full picture of the response of an
127 active sector of the GrIS to changing surface melt inputs.

128 **2 Methods**

129 2.1 Study Site

130 Isunnguata Sermia is a large land-terminating outlet glacier on the western margin of the GrIS,
131 situated in an overdeepened subglacial trough ~650 m deep (Lindbäck et al. 2014). Our field site
132 is ~800 m south of the trough and approximately 8 km from the terminus, in an area hypothesized
133 to contain multiple active subglacial lakes (Fig. 1a; Livingstone et al., 2019). Bed topography
134 measurements and subglacial routing from hydraulic potential predict a major subglacial
135 drainage axis through this trough (Fig. 1a; Livingstone et al., 2019; Pitcher et al., 2020). This axis
136 drains one of the largest land-terminating catchments in Greenland, routinely ranking among the
137 top five annual modelled runoff outlets of the GrIS (Fig. S4; Mankoff et al., 2020). Peak summer
138 subglacial discharge in the Isunnguata Sermia trough is estimated to be on the order of 10^3 $m^3 s^{-1}$
139 (Mankoff et al., 2020), approximately four orders of magnitude higher than the secondary, local
140 subglacial channels (10^{-2} $m^3 s^{-1}$) fed by the instrumented moulins.

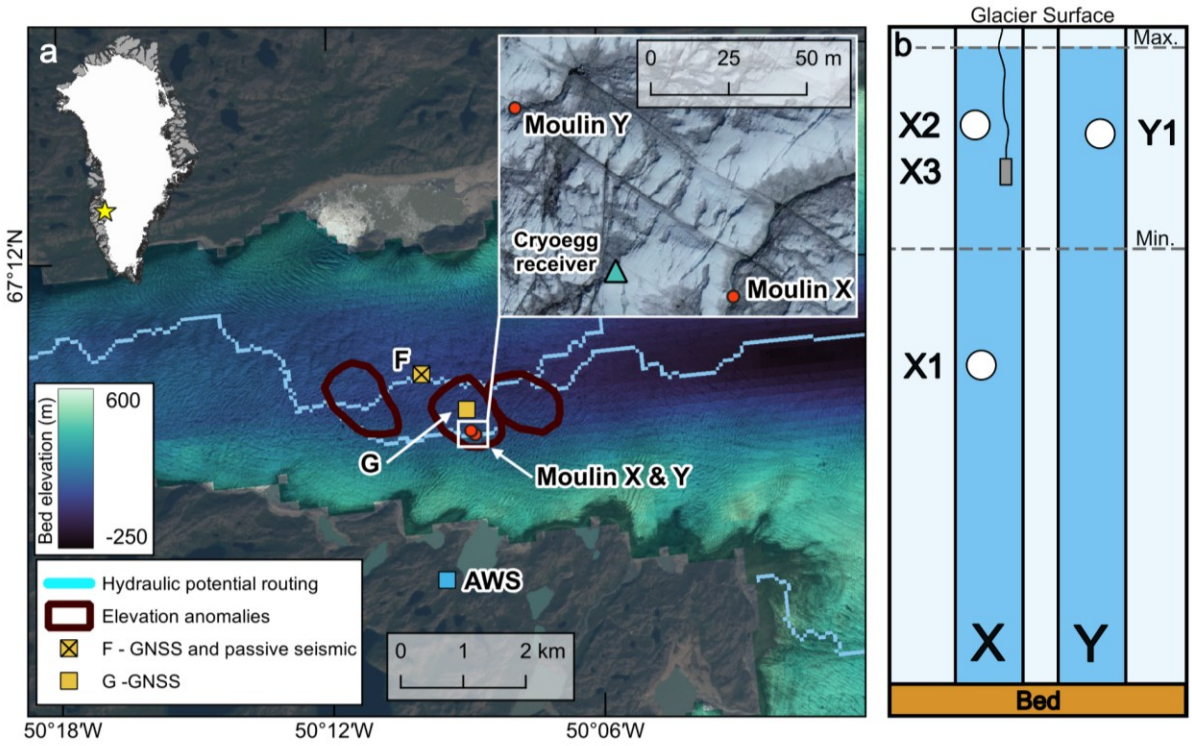

Figure 1. Study site on Isunnguata Sermia in southwest Greenland: (a) Overview of the study area, on a Sentinel-2 true-color image background. The shading represents the bed elevation from BedMachineV5 (Morlighem et al. 2022). Outlines of elevation anomalies (dark gray polygons) mark locations of suspected subglacial lakes (Livingstone et al. 2019) and the light blue line shows the dominant subglacial hydraulic potential routing. The inset on the top right shows a UAV true-color orthorectified image of instrumented Moulins X and Y. b) Schematic cross section of Moulins X and Y with estimated instrument locations (to scale in the vertical dimension), min/max moulin hydraulic head is denoted by the dashed lines.

2.2 Moulin instrumentation:

During July 2024, we instrumented two adjacent moulins (Moulins X and Y, Fig. 1a; 67° 10' N, 50° 10' W) above the margins of a suspected active subglacial lake (Livingstone et al. 2019) (Fig. 1a). Both moulins had an approximate radius at the surface of 2 m (Fig. S1) and small, poorly defined ice surface catchments of ~300 m^2. We estimated typical daily stream discharge into both moulins during the study period (July to August) to be about 0.03-0.06 m^3s^{-1} (Table S1).

Moulin X was instrumented on 12th July 2024 with a Geokon 4500SHSRX vibrating wire piezometer rated to 5 MPa attached to 400 m of cable with an integral high-tensile steel core. The Geokon piezometer was factory calibrated, and then zeroed in the field according to manufacturer's guidance to achieve accuracy of 0.1 bar. After calibration, the sensor was gradually lowered into the moulin until the pressure reading stopped increasing when additional cable was released; at which point the cable was anchored at the surface, with 300 m of cable

between the sensor and the ice surface. Water pressure and temperature were recorded at 15-minute intervals by a Campbell CR1000 logger via a AVW200 vibrating wire interface (Fig. S2c).

We also installed two Cryoegg wireless sensor systems (Prior-Jones et al. 2021), X1 and X2, on the 12th and 26th July 2024 respectively. Moulin Y, located ~90 m northwest from Moulin X, was instrumented with a single Cryoegg (Y1) on the 18th July. The Cryoeggs were deployed by dropping them into a moulin, where they descended via free-fall until becoming lodged or entering the moulin water column (Movie S1). Cryoeggs recorded the water pressure, EC and water temperature and transmitted their data wirelessly via VHF radio to a receiver on the ice surface at hourly intervals (Figure S2a). The Cryoegg pressure and temperature sensor (Keller 7LD, 100 bar) was factory calibrated, whilst the EC sensor was bespoke and calibrated with a dilution series of NaCl solution mixed with surface meltwater, cross-checked with a low-range conductivity meter (Hanna), specifically targeting the most likely range for ice melt (2-50 µS cm^{-1}). Supraglacial meltwater inputs are typically solute-poor with low EC (~0.1 to 5 µS cm^{-1}; Collins, 1979; Gordon et al., 1998), whereas water with subglacial origin can have a significantly higher EC (20 to 60 µS cm^{-1}; Tranter et al., 1997; Gordon et al., 1998) due to increased contact with subglacial sediments, bedrock and debris-laden ice, and subsequent chemical weathering (Stone and Clarke 1996), thus the sensor was calibrated to maximise sensitivity in these ranges. The surface receiver included a barometric pressure sensor (TE Connectivity MS506702BA03) to correct water pressure for atmospheric pressure variations, and an Iridium transceiver that transmitted all received data to a UK-based server every hour. The Cryoeggs were modified with a foam and mesh flotation device that increased their buoyancy asymmetrically, bringing them closer to neutral buoyancy (Figure S2b) to aid their transit through the englacial drainage system.

To obtain an estimate of sensor depth relative to the bed, we recorded the free-fall duration of Cryoegg Y1 before it impacted an ice ledge above the moulin's hydraulic head (confirmed by EC readings). Combining this measurement with ice thickness estimates from nearby ice penetrating radar surveys enabled calculation of Cryoegg Y1's height above the bed. By assuming hydraulic equilibrium between Moulins X and Y at a selected reference date (Fig. S3), we converted water depth to orthometric hydraulic head and water pressure to percentage of ice overburden (Text S1). Cryoegg X2 and Y1, and Geokon X3, were only submerged in water when hydraulic head was high, while Cryoegg X1 provided a full record of moulin hydraulic head. The EC time series from Cryoegg Y1 was anomalous, suggesting the sensor was damaged during deployment. Therefore, the measurements from this sensor are indicative, and only used to detect the transition between submerged and dry conditions.

2.3 Meteorological data:

Hourly surface meltwater production over our field site was modeled using COSIPY – a COupled Snowpack and Ice surface energy and mass-balance model in PYthon (see Sauter et al. 2020), forced by extrapolated data from the PROMICE KAN_L automatic weather station (AWS) (Fausto et al. 2021), which is situated approximately 12 km southeast of our field site at an elevation of ~630 m a.s.l. Air temperature was extrapolated to the elevation of our field site using a lapse rate of -5.3°C km^{-1} (Harper et al., 2011), and atmospheric pressure was corrected using a

barometric equation. Precipitation and snowfall data were extracted from the nearest ERA5-Land reanalysis grid cell (native resolution of 9 km, Muñoz Sabater et al. 2021). While simple extrapolation of variables limits the accuracy of absolute melt values over our field site, the temporal variation in surface melt provided useful insight into the timing and magnitude of surface water inputs into the subglacial hydrologic system. We also used air temperature data from an AWS deployed 3 km south of our field site (elevation of 515 m a.s.l.; AWS in Fig. 1a). This AWS does not measure all variables needed to force a surface energy balance model, hence the use of KAN_L for calculating surface melt. For investigating rainfall, we also use precipitation data measured by the land-based KAN_B weather station, located 6 km south of our field site.

2.4 Measurements of horizontal and vertical ice surface motion:

Time series of horizontal and vertical ice surface motion were determined from dual frequency (L1 + L2) Global Navigation Satellite System (GNSS) data recorded by Leica GS10 and GM30 receivers at 0.1 Hz. GNSS stations F (67° 11’ N, 50° 9’ W) and G (67° 10’ N, 50° 8’ W) were located 1.2 km and 0.35 km from Moulin Y respectively (Fig. 1). GNSS antennas were mounted on 6-m-long aluminium poles drilled 5 m into the ice surface. Rapid re-freezing of the hole secured the antenna pole within the ice. Data were post-processed kinematically (King, 2004) relative to a bedrock-mounted reference station using the differential carrier-phase positioning software Track v1.53 (Chen, 1998). Baseline lengths were <4 km and precise ephemerides from the International GNSS Service were used (Dow et al., 2009). Positioning uncertainties were estimated at ~0.01 m in the horizontal and ~0.02 m in the vertical by calculating the standard deviation of the residuals from linear regression applied to the position time series during a month-long period of steady ice motion in November 2023. Small (<5 min) gaps in the position record were linearly interpolated before a second-order 6 h low-pass Butterworth filter was applied. The position record was then resampled to 10-minute medians and differentiated to calculate velocity, which was further filtered using a 6 h moving average. To prevent phase shifts, phase-preserving filters, differentiation, and resampling methods were used throughout. Vertical displacement due to advection over varying bed topography was removed by calculating local bed slope angles during stable winter periods (Hooke et al., 1989; Andrews et al., 2014). To account for changing topography throughout the season, bed slope values were linearly interpolated between calculations made before and after the 2024 melt season. These calculations assume that basal sliding accounts for 96 % of the surface velocity measured by the GNSS receivers (Maier et al., 2019) and that vertical displacement from cavity opening or overburden pressure changes is negligible during non-melt season periods.

2.5 Measurements of glacio-hydraulic seismic tremor

To characterize water flow in the subglacial drainage system we installed a seismometer at site F (Fig. 1) comprising a C100 Geobit borehole geophone with a corner frequency of 4.5 Hz drilled to 5 m depth and logged by a Digos DATA-CUBE^3 at 100 Hz. Measurements of glacio-hydraulic seismic tremor in alpine glaciers (Bartholomaus et al. 2015; Gimbert et al. 2016; Nanni et al. 2020) and in Greenland (Mejia et al. 2022) have been used as a proxy for subglacial discharge and water pressure. Seismic power was calculated by performing Welch’s method over 3 s time windows

with 50% overlap (Welch, 1967) on the vertical component of ground motion. This time window was chosen to minimise the influence of short-duration, but high energy, events such as icequakes. To isolate the seismic tremor caused by subglacial discharge, the mean power between 2 and 10 Hz (Bartholomaus et al. 2015; Gimbert et al. 2016) over 60 s time windows was calculated and displayed in decibels (dB; decimal logarithmic).

3 Results

Between 18th July and 31st August 2024, the catchment exhibited five distinct periods of hydrological behavior. These periods were grouped into two modes that had similarities in the relationship between surface melt, ice velocity, glacio-hydraulic seismic tremor, moulin hydraulic head and moulin EC. During Mode 1 moulin head and ice velocity co-vary (periods 1, 3 and 5; pale red shading Fig. 2); while during Mode 2 moulin head exhibits large diurnal variations while ice velocity and seismic tremor remain relatively stable or decrease towards background levels (periods 2 and 4; blue shading Fig. 2).

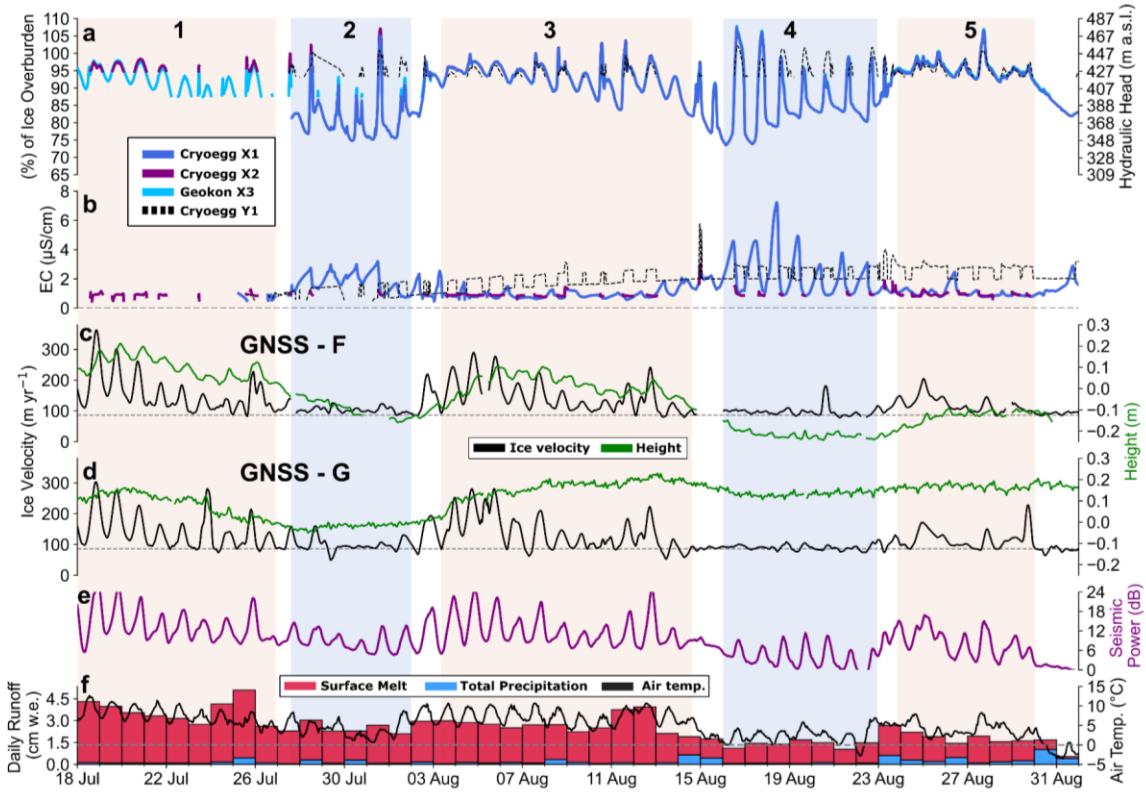

Figure 2: Supra- and englacial measurements from summer 2024. a) Hydraulic head in Moulin X and Y. b) Electrical conductivity in Moulin X and Y. c) GNSS-derived ice velocity (black) and height (green) for GNSS F. d) Same as c) for GNSS G. e) Mean seismic power at F for the frequency range 2 to 10 Hz. f) Modeled daily melt (red bars), daily rainfall from KAN_B weather station (blue bars) and hourly air temperature at the AWS (black). Bold numbers on (a) denote identified periods discussed in the text. Pale red shading highlights periods of Mode 1 behavior and pale blue

periods of Mode 2 behavior. The horizontal dashed gray line on (c) and (d) marks denotes the median winter ice velocity for G. Time is West Greenland Summer Time (UTC -2).

Period 1 (18th to 27th July 2024):

Period 1 was characterized by strong diurnal fluctuations of surface melt, ice velocity, seismic tremor and moulin hydraulic head (Fig. 2). Peak moulin hydraulic head, ice velocity, surface height and seismic tremor all lagged peak daily surface melt. The mean lag time with respect to melt varied from 6.7 ± 2.3 hours for hydraulic head, 5.6 ± 1.8 hours for ice velocity at G and F, 10.0 ± 1.6 hours for surface height at F and 8.5 ± 1.3 hours for seismic tremor (Fig. 3c-f). Moulin X hydraulic head averaged ~94% of ice overburden pressure (~420 m a.s.l. hydraulic head) with smooth diurnal variations of approximately 6 to 8% of ice overburden (~25 m hydraulic head) (Fig. 2a), whilst ice velocity exhibited diurnal variations of up to ~200 m yr^{-1} at F and G (Fig. 2c-d). Between the 21 and 24 July, the daily mean moulin hydraulic head decreased, with the water level falling below the Geokon X3 sensor level (equivalent to ~ 86% of ice overburden) for ~10 hours overnight between 22nd and 27th July (Fig. 2a). This reduction in head coincided with decreasing daily surface melt, a generally decreasing diurnal amplitude of ice velocity from ~200 m yr^{-1} to 50 m yr^{-1} (Fig. 2c), and declining seismic tremor at F (Fig. 2e). GNSS F, located over a predicted major subglacial drainage route, exhibited diurnal variations in surface height of ~8 cm day^{-1}, and had a background decrease in height of 20 cm (Fig. 2c), whilst GNSS G showed muted diurnal variation but underwent a gradual 21 cm decrease in vertical position (Fig. 2d). EC showed no resolvable variation during this period, with values of ~1 µS cm^{-1} (Fig. 2b).

Period 2 (28th July to 3rd August 2024):

Following two days of elevated surface melt on 24th and 25th July (~4 cm w.e. day^{-1}, Fig. 2f), daily melt rates declined and the diurnal melt cycle became less distinct. This reduction in surface melt marked the onset of a shift in dynamic and hydrological behavior, during which ice velocity decoupled from the diurnal surface melt cycle. During period 2, the lag times for ice velocity and surface height were highly variable or absent due to the muted diurnal variations (Fig. 3c-e). In contrast, the lag time for the moulin hydraulic head decreased to 1.3 ± 0.9 hours, while EC became inversely correlated, peaking 21.5 ± 1.3 hours after peak melt (Fig. 3a-b). Diurnal variations in head at Moulin X became more pronounced, with an initial rapid increase from 75 % to 105 % of ice overburden pressure over 6 hours, followed by a decrease to 80% of ice overburden pressure over 3 hours, and then a more gradual decrease overnight to 74% over 14 hours. The maximum diurnal range was ~30 % of ice overburden, with pressures reaching a minimum of 75% and occasionally exceeding ice overburden pressure (Fig. 2a), notably different to Period 1. This variation in head occurred with no associated increase in height or horizontal ice displacement at G or F, and ice velocities decreased to the winter median or lower (Fig. 2c-d). Tremor at F exhibited a gradual decline with a smaller diurnal amplitude (Fig. 2d) and a reduced lag time, peaking 5.95 ± 2.5 hours after peak surface melt (Fig. 3f) . EC exhibited a strong, lagged inverse correlation with hydraulic head and melt. For example, EC at Cryoegg X1 (~200 m above the bed) displayed distinct diurnal variations superimposed on a gradual increase over ~17 hours (up to ~2.5 µS cm^{-1}) as moulin hydraulic head decreased and stabilized. This was followed by a

rapid decline over ~5 hours as the hydraulic head rose again with the influx of surface meltwater on 31st July (Fig. 2a). The daily minimum EC values remained elevated (> 1.5 µS cm^{-1}) from 28th to 31st July, with later minimum daily values generally <1 µS cm^{-1}.

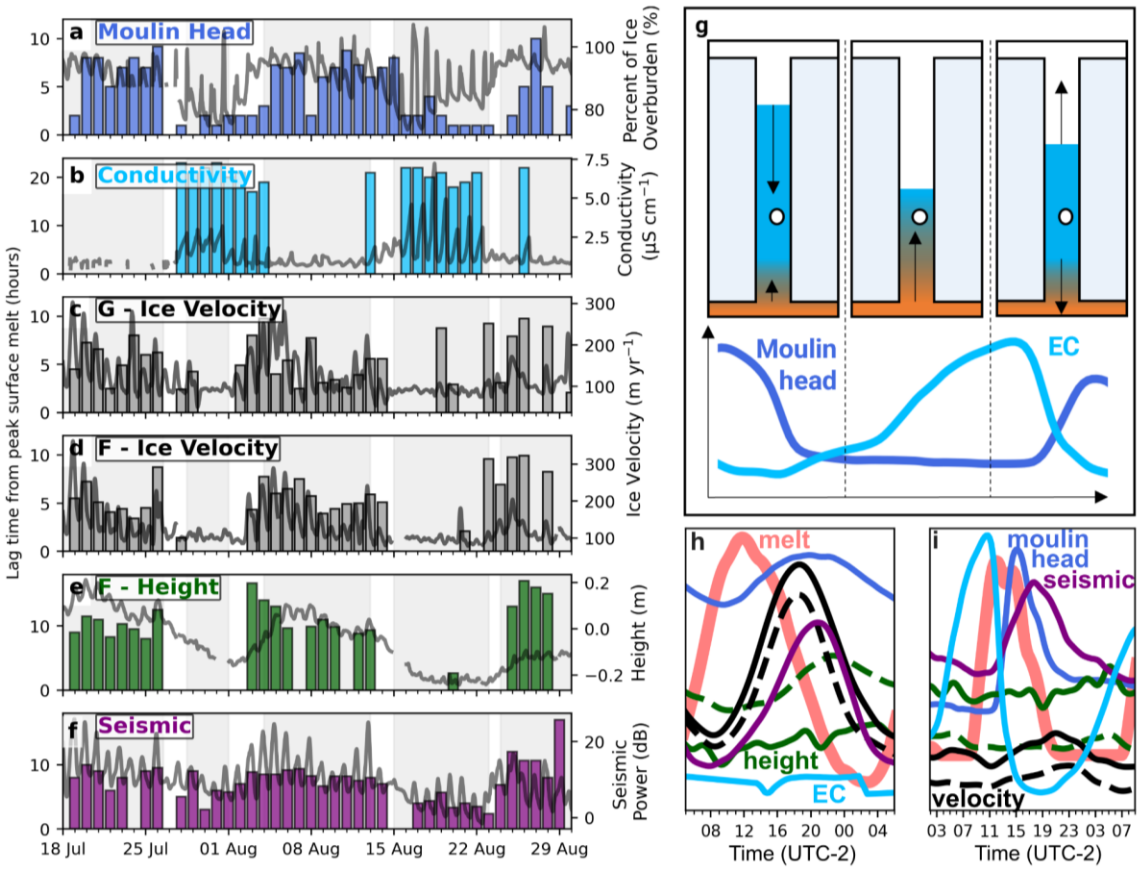

Figure 3: (a–f) Lag times (hours) between daily peaks in surface meltwater production and subsequent peaks in measured variables (bars, left axis). Solid gray lines denote the variation of each variable (right axis). (g) Conceptual model of the diurnal cycle of moulin head and electrical conductivity during a disconnected period (plot shows 17th to 18th July 2024). (h and i) Normalized time series comparing (h) connected (periods 1, 3 and 5) and (i) disconnected drainage periods 2 and 4. Line colors for each variable are consistent with plots (a to f). Height and velocity is shown by a solid line for G and dotted line for F.

Period 3 (3rd to 14th August 2024):

With increased daily surface melt from the 1st to 2nd August (from 2.0 to 2.8 cm w.e. day^{-1}; Fig. 2f), the well-coupled behavior observed in Period 1 returned, characterized by large diurnal variations in all variables apart from EC (Fig. 2). This re-coupling was also evident in the lag times between peak surface melt and peaks in moulin hydraulic head at 6.3 ± 2.2 hours, ice velocity at F and G at 5.3 ± 1.8 hours, surface uplift at F at 10.7 ± 1.9 hours, and seismic tremor at F at 8.2 ± 0.7 hours (Fig. 3a-f). Moulin X hydraulic head had a mean of ~93% of ice overburden. While the initial diurnal range was ~5%, like Period 1, the variability increased in the latter half of the period to ~15% as surface melt and ice velocity decreased. The almost identical diurnal variations in hydraulic head at Moulin X and Y suggests they were hydraulically well connected (Fig. 2a). On

several days (e.g., 7th to 10th August), moulin hydraulic head showed a double-diurnal peak, with an initial spike followed by a secondary sinusoidal curve. Over four days from 2 to 6 August, GNSS F and G increased in height, by 26 cm and 16 cm respectively. Site F showed diurnal variations in surface uplift of 6 to 8 cm (Fig. 2c), while no well-defined diurnal variation was present at G (Fig. 2d) and EC remained low (<1 µS cm^{-1};Fig. 2b).

Period 4 (15th to 23rd August 2024):

Daily surface melt decreased significantly from ~4 cm w.e. day^{-1} on 12th August to ~1.5 cm w.e. day^{-1} by 14th August (period 4; Fig. 2f). This coincided with air temperatures dropping below freezing on 16 August for the first time in the study period (Fig. 2f). Ice velocity and surface uplift at G and F were characterized by muted diurnal variability, and their vertical positions decreased by 13 and 23 cm respectively from 13th to 18th August (Fig. 2c-d). As melt decreased, moulin hydraulic head initially exhibited increased diurnal variability, which decreased throughout the period due to the convergence of maximum and minimum values (Fig. 2a). The hydraulic head averaged ~85% of ice overburden during period 4, with a diurnal range of nearly 33%, and exceeded ice overburden pressure on 17th and 18th August (Fig. 2a). The diurnal pattern of hydraulic head resembled Period 2, with a rapid increase followed by a two-step decrease. When submerged, Cryoegg Y1 recorded a similarly high hydraulic head in Moulin Y, with its daily maximum exceeding that of Moulin X by up to 10% of ice overburden pressure (~40 m hydraulic head) from 18th to 23rd August (Fig. 2a). EC exhibited a rapid shift in behavior with pronounced diurnal variations of 3 µS cm^{-1} up to a maximum daily value of ~7 µS cm^{-1}, inversely correlated with the hydraulic head (Fig. 2b). Moulin hydraulic head had a lag time of only 1.8 ± 1.0 hours, EC of 20.4 ± 1.5 hours and seismic tremor of 3.9 ± 1.0 hours from peak surface melt (Fig. 3a-f).

Period 5 (24th to 30th August 2024):

On 24th August, rising air temperature led to increased and more variable overnight surface melt, contrasting with the cessation of melt during the nights of the preceding period (Fig. 2f). This shift triggered increased variability in seismic tremor at F (Fig. 2e), followed by greater variations in ice velocity at both G and F, alongside a 20 cm rise in surface height at F (Fig. 2c). In contrast, the height at G remained relatively stable (Fig. 2d). Less pronounced diurnal variability of surface melt rendered the lag times highly variable and difficult to discern (Fig. 3a-f). Between 22nd and 26th August, sustained overnight surface melt resulted in a high and stable moulin hydraulic head at both Moulin X and Y, maintaining ~95% of ice overburden pressure with variations of <5% (Fig. 2a). Diurnal variations in EC remained muted, stabilizing at around 1 µS cm^{-1} (Fig. 2b), except for a 0.5 µS cm^{-1} increase on 26th August, coinciding with a day of low surface melt. After an increase in daily surface melt on 27th August, moulin hydraulic head briefly exceeded ice overburden pressure, followed by an increase in ice velocity at G and F (Fig. 2c-d). On 30th August, a decline in daily surface melt (Fig. 2f) drove a linear decrease in moulin hydraulic head from 95% to 80% of ice overburden pressure over a two-day period (Fig. 2a). This was coincident with a large speed-up event at G (but not F), which was unrelated to surface melt forcing (Fig. 2d).

4 Discussion

The behavior exhibited during the five time periods was grouped into two characteristic hydrological modes that we classify as 'connected' (Mode 1), periods of regional-catchment dominated drainage where most variables co-vary (periods 1, 3 and to a certain extent, 5) and 'disconnected' (Mode 2), indicating more localized controls on drainage (periods 2 and 4). We attribute the rapid (<24 h) switching between these modes to interaction between the local secondary drainage system beneath the instrumented moulins and the larger, primary subglacial drainage axis located within the deep subglacial trough.

To differentiate between these different scales of drainage, we hereafter use the terms "primary" and "secondary" to refer to the subglacial drainage features, and "regional" and "local" to describe their respective catchments. The primary drainage axis is defined by the major subglacial drainage route that drains the main regional catchment up-glacier of our study site (~ 14,000 km^2; Mankoff et al., 2020), which is situated in the deep subglacial trough. The secondary (or subsidiary) channels are smaller conduits fed by a local catchment (typically ~ 300 m^2), represented by the instrumented moulins. This distinction allows us to differentiate between large-scale glacio-hydraulic response and local variations in subglacial water pressure.

Glaciological setting of the instruments

The passive seismic sensor and GNSS at F are located over the ~650-m-deep subglacial trough (Lindbäck et al. 2014), near a predicted major subglacial drainage route (Figs 1c, 4). We expect the seismic tremor at F (Fig. 2e) to represent the hydraulic characteristics of this drainage route, with high seismic power between 2 and 10 Hz indicating high subglacial discharges and/or turbulent flow driven by hydraulic gradients (Bartholomaus et al. 2015; Gimbert et al. 2016). In contrast, variations in ice velocity (Fig. 2c-d) are interpreted as a response to changes in basal sliding modulated by averaged regional basal water pressure (Iken and Bindschadler, 1986; Kamb et al., 1994). GNSS G was located ~400 m southeast of F above the centre of a purported active subglacial lake identified from elevation anomalies in satellite altimetry data (Livingstone et al., 2019; Figs. 1a, 4). Moulins X and Y were located approximately 800 m away from the main drainage route, on the edge of the elevation anomaly of the active subglacial lake (Fig. 4).

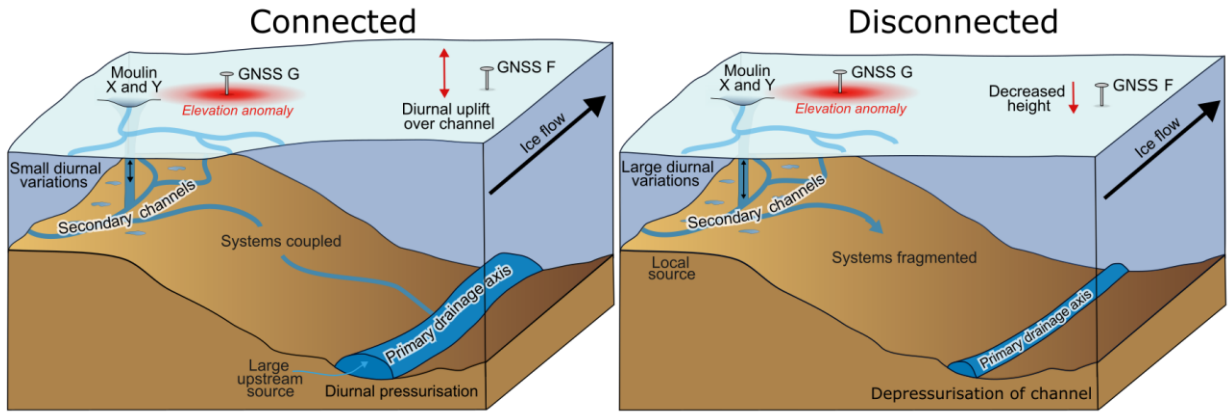

Figure 4. Schematic cross-section of study site for (a) connected periods and (b) disconnected periods. Ice flow is into the page. Figures are not to scale.

Proximity to the primary subglacial drainage axis, and the extent of the channelization, controls the response of the measured variables to changes in surface water inputs. During high melt periods, ice velocity, surface uplift and seismic tremor at F (Fig. 2c and 2e) exhibit strong diurnal cycles, related to increasing discharge and daily pressurization in the primary drainage axis as surface meltwater inputs from the wider catchment are routed through the trough. Further away at G (Fig. 2d), ice velocity shows a strong response but the diurnal cycle of surface uplift associated with pressurization of the primary drainage route is muted (Fig. 4). Moulin hydraulic head is episodically in phase with ice velocity (i.e. during 'connected' periods), but there are also 'disconnected' periods where water pressure exceeds ice overburden pressure with no associated increase in ice velocity or surface uplift at GNSS F or G (e.g., 31st July, 16th and 17th August; Fig. 2a). This illustrates the complex response of the ice surface to subglacial hydrological events in a small region: the ice velocity at G and F, along with the seismic tremor at F, reflect regional ice motion controlled by the primary subglacial drainage axis near F (Fig. 4). In contrast, while hydraulic head in Moulins X and Y (Fig. 2a) periodically co-varies with the diurnal ice motion and seismic tremor variations observed at F and G, at other times (e.g., periods 2 and 5) they respond to local surface water inputs. This, in tandem with similar observations where the relationship between hydraulic head and ice velocity varies according to connectivity with the drainage system in Greenland (Andrews, et al. 2014) and beyond (Rada and Schoof, 2018; Rada and Schoof 2023), suggests hydrological switching controlled by local (<1 km^2) or regional (> 1 km^2, and potentially glacier-scale) responses to melt.

Connected, efficient subglacial drainage responds to regional events:

The strong diurnal fluctuations in ice motion at F and G during 'connected' periods 1 and 3 (Fig. 2c-d) are indicative of an efficient, channelized subglacial drainage system, as observed by other studies in the ablation zone of the GrIS (Andrews et al. 2014; Cowton et al., 2016; Mejia et al., 2021; Chandler et al., 2021). Diurnal variability in surface melt causes pressurization of the primary subglacial drainage axis and surrounding hydraulically connected drainage system (Hubbard et al., 1995; Gordon et al., 1998), reducing basal friction and thus increasing velocity.

Transient pressurization of the primary drainage axis explains the strong diurnal surface uplift at F (Fig. 2c), a behavior well-documented in other studies (Shepherd et al., 2009; Iken & Bindschadler, 1986; Nienow et al., 2005; Sugiyama et al., 2008). In contrast, surface uplift at G (Fig. 2d) does not have a strong diurnal cycle but rather displays a period-dependent cycle comprising increased uplift during periods 1 and 3 and decreased uplift in periods 2 and 4 (Fig. 2d). Since G is further away from the primary subglacial drainage axis (Fig. 1 and 4), the effects of pressurization are dampened. This is consistent with observations from Tedstone et al., (2014) that show distributed drainage can readily interact with channelized features, smoothing out spatial variations in velocity caused by pressure fluctuations within the channel.

The large lags between peak surface melt and ice velocity at F and G (~5 hours, Fig. 3) and seismic tremor (~8 hours, Fig. 3) suggests that the system is driven by a large, upstream water source (Chandler et al., 2021; Mejia et al. 2022). This behavior aligns with the large scale of the Isunnguata Sermia catchment, which ranks among the top five largest runoff outlets of the entire ice sheet (Fig. S4; Mankoff et al., 2020). In comparison, the nearby Leverett Glacier has a substantially smaller catchment and typically exhibits a smaller lag between surface melt and ice velocity of 2 to 3 hours (Shepherd et al. 2009; Bartholomew et al. 2011). The ~3 h difference in lag time between ice velocity and seismic tremor may be because the velocity is associated with the greatest rate of change of melt input (i.e. the rising limb), but tremor peaks at the subglacial discharge maxima.

The moulin hydraulic head variations during periods 1 and 3 (Fig. 2a) align closely with the diurnal behavior recorded by the instruments at F and G (Fig. 2c-d). Compared to inferred efficient, channelized moulin head variations reported in Andrews et al., (2014), the diurnal variations reported here show a smaller diurnal range and higher average. We attribute this difference to the smaller size of our instrumented moulins and the associated channelized subglacial drainage system, which exhibits less capacity to accommodate diurnal fluctuations in subglacial discharge. The sinusoidal diurnal cycle in hydraulic head, with a large lag between peak surface melt and hydraulic head (~6 hours, Fig. 3a), is interpreted to reflect the smoother regional discharge signal (Chandler et al., 2021; Mejia et al. 2022). This implies that during the 'connected' periods, Moulin X is hydraulically linked to the primary subglacial drainage axis , as locally derived meltwater would typically produce a more immediate response in both water pressure and EC during the efficient late-melt season, as seen in periods 2 and 4 (Fig. 4a). However, some days are characterized by two peaks (e.g., 8th August, Fig. 2a), with an earlier rapid spike likely representing locally-sourced surface meltwater inputs preceding the regional signal. There is an anti-clockwise hystereses between surface melt and ice velocity, seismic tremor, and moulin head (Fig. S5) demonstrating modulation of the system by upstream water (Chandler et al., 2021). The low EC with limited variability suggests an efficient, channelized drainage system with low residence times (Rada & Schoof, 2018). Consequently, we infer that the EC signal is dominated

by supraglacial inputs into the moulin rather than water that has had prolonged contact with the bed (Gordon et al., 1998).

Local, disconnected drainage:

At the start of time periods 2 and 4, a 50% and 70% decrease in daily surface melt (Fig. 2f), respectively, triggered a rapid shift in system behavior. The gradual decline in seismic tremor (Fig. 2e) with subdued diurnal variations indicates a reduction in discharge and / or water pressure (Nanni et al. 2020), consistent with a subglacial drainage route that is now largely able to accommodate the reduced melt inputs. The gradual drop in surface height at F and G (Fig. 2c-d)indicates depressurization of the main drainage route and surrounding cavities hydraulically connected to it, leading to increased basal traction and reduced sliding (Hoffman et al., 2011; Mair et al., 2001; Iken and Truffer, 1997). This behavior is consistent with the decrease in ice velocity to below the winter median (van de Wal et al. 2008; 2015; Sole et al. 2013; Fig. 2c-d).

The moulin hydraulic head during periods 2 and 4 exhibits large diurnal variations, frequently reaching ice overburden pressure, without a corresponding increase in vertical or horizontal ice motion response at G (Fig. 2a). Combined with the reduced lag time (~2 hours; Fig. 4a), which points to a direct, local meltwater source, we interpret this behavior to indicate Moulins X and Y becoming hydraulically disconnected from the primary subglacial drainage axis or other upstream sources, and instead exhibit local variations in subglacial hydrology. This interpretation is further supported by differences in maximum daily hydraulic head (e.g., 31st July–2nd August and 18th–23rd August; Fig. 2a) occasionally observed between moulins X and Y, despite their proximity (50 m apart). These differences suggest they are occasionally hydraulically disconnected from each other and it is therefore unsurprising that they are also disconnected from the main channel (Holmlund and Hooke 1983; Holmlund 1988). Fragmentation of hydrological features is likely to occur both hydraulically and mechanically due to the increased effective stress (bridging stresses) as the main drainage route depressurizes (Weertman, 1972). These disconnected periods are similar to the 'switching behaviors' observed in previous studies, where isolated cavities connect and disconnect from the main channelized system (Fudge et al., 2008; Gordon et al., 1998; Murray & Clarke, 1995; Rada & Schoof, 2018; Andrews et al., 2014).

The larger diurnal fluctuations in EC during periods 2 and 4 show the influence of meltwater that has had increased contact time with subglacial sediments (Gordon et al., 1998, 2001). Asymmetric moulin hydraulic head (Fig. 3i) and longer residence times indicate the transient storage and release of meltwater within the sediments and cavities surrounding the local subglacial channel (Hubbard et al., 1995), a scenario simulated by gradual leakage of water from weakly connected components of the subglacial drainage system (Hoffman et al., 2016). As moulin hydraulic head increases during the day, the resulting high pressure forces water into an inefficient distributed system adjacent to the local subglacial channel. When surface melt inputs decrease, hydraulic head drops rapidly. This decline is characterized by two distinct phases: a rapid initial drop in head reduces pressure in both the moulin and the connected subglacial channel, during which the moulin EC remains static and low (Fig. 3g); followed by a slower decrease overnight as the moulin begins to equilibrate with the pressure of the adjacent

distributed system. During this slower decline, the decrease in channel pressure reverses the hydraulic gradient, releasing subglacial water that had been forced into the distributed system earlier in the day (Hubbard et al., 1995) (Fig. 3g). This process, which can involve Darcian flow through subglacial sediments, returns solute-rich water from the adjacent distributed system into the channel. This water subsequently diffuses up the moulin water column, thereby increasing the EC measured at the sensor location (Gordon et al., 1998).

Implications for understanding ice sheet hydrology

The surface topography of the lower ablation area of Isunnguata Sermia is notable for the large number of small (<3 m diameter) moulins (Jones et al. 2018), which generally have small catchments (<300 m^2). The transient nature of these surface-to-bed connections, combined with limited surface melt inputs, and the high density of moulins delivering meltwater to the bed, hinders the development of larger hydrological catchments that could support a well-established, local channelized subglacial drainage system in this region (Banwell et al. 2016). While large diurnal variations in water pressure occur within these local moulins, they have little impact on ice velocity. Instead, ice velocity is dominated by the influence of the primary subglacial drainage axis and the regional background water pressure, which suggests the configuration of the local secondary subglacial drainage system has a negligible impact on the spatial pattern of summer ice motion (Tedstone et al., 2014). Consequently, the local secondary channels act independently of the regional system when melt is low, but become connected into the broader network at higher subglacial discharge.

We demonstrate that connectivity between primary and secondary drainage systems beneath the margins of the GrIS changes rapidly and repeatedly in response to both varying daily melt rates and the evolving capacity of the regional network. Despite the location of the monitored moulins, ~800 m from the primary drainage axis along the subglacial trough (Fig. 4), their hydraulic head was frequently influenced by the regional subglacial drainage response. This behavior is consistent with the primary subglacial drainage axis becoming overwhelmed and forming connections to the local secondary channels (Rada and Schoof, 2018; 2023), demonstrating that subglacial channel(s) can have a broad lateral influence on hydrological behavior. The much larger variations in surface melt and subglacial discharge at this site mean that the lateral scale of connectivity (100s meters) is significantly greater than the <100 m scale estimated from borehole arrays on smaller glaciers (Hubbard et al., 1995; Gordon et al., 1998; Fudge et al., 2008; Rada and Schoof 2018; 2023). These lateral bounds are also consistent with the width of meltwater corridors identified in palaeo-ice-sheet settings, supporting the interpretation that these features are the geomorphic expression of hydraulic connectivity (Lewington et al., 2020).

Conversely, during cooler periods, the influence of the primary subglacial drainage axis contracts (Fig. 4b)) as the efficient drainage system that has evolved through the melt season is able to accommodate the smaller, less variable melt inputs. This leads to fragmentation of the previously channelized drainage system surrounding the primary drainage axis into hydraulically disconnected and locally-influenced subsystems. While the moulins capture the sensitivity of the

local secondary system to changes in runoff, and frequently experience water pressures exceeding ice-overburden pressure, this has minimal influence on ice motion. Regional ice motion is predominantly controlled by the pressure and extent of the primary drainage axis, regardless of local pressure highs in the secondary channels. Therefore, moulin records should not be interpreted in isolation, but rather within the context of their connectivity to the regional drainage system. Our data demonstrate how secondary channels can behave independently; thus in these settings, moulin records are best viewed as a manometer of local connectivity, providing context for interpreting coincident changes, or lack thereof, in ice velocity (Mejia et al. 2021). Further insights into these complex hydraulic interactions could also be gained through a dedicated analysis of lag times across different hydrological variables (Mejia et al., 2022). Longer-term records are particularly useful in this context (Rada and Schoof, 2018), especially if supported by other indicators of meltwater residence time such as EC. The use of wireless instruments such as Cryoegg (Prior-Jones et al. 2021) enables capture of these long-term data with fewer logistical challenges than cabled sensors, and satellite telemetry of data provides the functionality to monitor drainage system behaviors in near-real time.

5 Conclusions

Our observations of moulin water pressure, residence time (EC), ice motion (horizontal and vertical velocity) and glacio-hydraulic tremor demonstrate the presence of a local secondary channel(s) that periodically connect to the wider, primary subglacial drainage axis. Connectivity between these two systems switches rapidly (hourly timescales) and frequently (twice during this six-week dataset) in response to variations in melt input. The repeated disconnection of the secondary channel(s) from the primary drainage axis provides evidence of fragmentation between drainage systems on the GrIS. When disconnected (mode 2), local secondary channels become hydraulically isolated (Fig. 4b) and experience large water pressure variations, frequently exceeding ice overburden, that have minimal impact on regional ice velocity. Instead, regional ice dynamics is controlled by the pressure and extent of the large primary subglacial drainage axis adjacent to the catchment, whose lateral influence stretched at least 800 m (more than one ice thickness) from the trough (Fig. 4). This disconnection challenges the assumption that individual moulin and borehole pressure records can serve as direct proxies for regional subglacial drainage conditions. These findings indicate that large primary drainage axes are the fundamental drivers of regional ice dynamics in Greenland, and are capable of obscuring the effects of local pressurisation in secondary channels. While these secondary channels play a minimal role in driving regional ice flow, observing their behavior and connectivity to wider systems provides useful context for process-based modelling of subglacial systems.

Inclusion in Global Research Statement

The research presented in this study was conducted in Greenland, in the Aasivissuit-Nipisat UNESCO world heritage site, over multiple field campaigns. All fieldwork was conducted under relevant science expedition permits issued by the Greenland government (Ministry of Environment and Nature). We are particularly grateful to the logistical and field support provided by Chris Sorensen and the staff at the Kangerlussuaq International Science Support centre, whose local expertise were vital to the successful and safe completion of our fieldwork.

Acknowledgments

The SLIDE team was supported by NERC Grant NE/X000257/1. The GNSS at F was provided by the Natural Environment Research Council (NERC) Geophysical Equipment Facility (loan 1143). RI was supported by a NERC PhD studentship (NE/T00939X/1). MPJ, JDH, LC, SFM and the Cryoegg equipment were supported by a UKRI Future Leaders Fellowship (to MPJ, MR/V022237/1). We acknowledge the support of Kangerlussuaq International Science Support and the local knowledge and guidance of Chris Sorenson.

Open Research

The moulin hydraulic head, GNSS-derived ice motion, passive seismic, and meteorological data will be deposited at the UK Polar Data Centre upon acceptance of this manuscript . The PROMICE weather station data sets are available from How et al., (2022). The liquid ice discharge data are available at Mankoff et al., (2020). The BedMachine v5 dataset is available from Morlighem et al. (2022).

Conflict of Interest Disclosure

The authors declare there are no conflicts of interest for this manuscript.

References

Andrews, L. C., Catania, G. A., Hoffman, M. J., Gulley, J. D., Lüthi, M. P., Ryser, C., et al. (2014). Direct observations of evolving subglacial drainage beneath the Greenland Ice Sheet. *Nature*, *514*(7520), 80–83. https://doi.org/10.1038/nature13796

Banwell, A., Hewitt, I., Willis, I., & Arnold, N. (2016). Moulin density controls drainage development beneath the Greenland ice sheet. *Journal of Geophysical Research: Earth Surface*, *121*(12), 2248–2269. https://doi.org/10.1002/2015JF003801

Bartholomaus, T. C., Amundson, J. M., Walter, J. I., O'Neel, S., West, M. E., & Larsen, C. F. (2015). Subglacial discharge at tidewater glaciers revealed by seismic tremor. *Geophysical Research Letters*, *42*(15), 6391–6398. https://doi.org/10.1002/2015GL064590

Bartholomew, I. D., Nienow, P., Sole, A., Mair, D., Cowton, T., King, M. A., & Palmer, S. (2011). Seasonal variations in Greenland Ice Sheet motion: Inland extent and behaviour at higher elevations. *Earth and Planetary Science Letters*, *307*(3), 271–278. https://doi.org/10.1016/j.epsl.2011.04.014

Brown, G. H., Sharp, M. J., Tranter, M., Gurnell, A. M., & Nienow, P. W. (1994). Impact of post-mixing chemical reactions on the major ion chemistry of bulk meltwaters draining the haut glacier d'arolla, valais, Switzerland. *Hydrological Processes*, *8*(5), 465–480. https://doi.org/10.1002/hyp.3360080509

Chandler, D. M., Wadham, J. L., Nienow, P. W., Doyle, S. H., Tedstone, A. J., Telling, J., et al. (2021). Rapid development and persistence of efficient subglacial drainage under 900

m-thick ice in Greenland. *Earth and Planetary Science Letters*, *566*, 116982. https://doi.org/10.1016/j.epsl.2021.116982

Chen, G. (1998). *GPS kinematic positioning for the airborne laser altimetry at Long Valley, California* (Thesis). Massachusetts Institute of Technology. Retrieved from https://dspace.mit.edu/handle/1721.1/9680

Clarke, G. K. C. (1987). Subglacial till: A physical framework for its properties and processes. *Journal of Geophysical Research: Solid Earth*, *92*(B9), 9023–9036. https://doi.org/10.1029/JB092iB09p09023

Collins, D. N. (1979). Quantitative Determination of the Subglacial Hydrology of Two Alpine Glaciers. *Journal of Glaciology*, *23*(89), 347–362. https://doi.org/10.3189/S0022143000029956

Cowton, T., Nienow, P., Sole, A., Wadham, J., Lis, G., Bartholomew, I., et al. (2013). Evolution of drainage system morphology at a land-terminating Greenlandic outlet glacier. *Journal of Geophysical Research: Earth Surface*, *118*(1), 29–41. https://doi.org/10.1029/2012JF002540

Cowton, T., Nienow, P., Sole, A., Bartholomew, I., & Mair, D. (2016). Variability in ice motion at a land-terminating Greenlandic outlet glacier: the role of channelized and distributed drainage systems. *Journal of Glaciology*, *62*(233), 451–466. https://doi.org/10.1017/jog.2016.36

Covington, M. D., Gulley, J. D., Trunz, C., Mejia, J., & Gadd, W. (2020). Moulin Volumes Regulate Subglacial Water Pressure on the Greenland Ice Sheet. *Geophysical Research Letters*, *47*(20), e2020GL088901. https://doi.org/10.1029/2020GL088901

Dow, J. M., Neilan, R. E., & Rizos, C. (2009). The International GNSS Service in a changing landscape of Global Navigation Satellite Systems. *Journal of Geodesy*, *83*(3), 191–198. https://doi.org/10.1007/s00190-008-0300-3

Doyle SH and others (2013) Ice tectonic deformation during the rapid in situ drainage of a supraglacial lake on the Greenland Ice Sheet. The Cryosphere 7(1), 129–140. doi:10.5194/tc-7-129-2013.

Doyle, S. H., Hubbard, B., Christoffersen, P., Law, R., Hewitt, D. R., Neufeld, J. A., et al. (2022). Water flow through sediments and at the ice-sediment interface beneath Sermeq Kujalleq (Store Glacier), Greenland. *Journal of Glaciology*, *68*(270), 665–684. https://doi.org/10.1017/jog.2021.121

Doyle, S. H., Hubbard, B., Christoffersen, P., Young, T. J., Hofstede, C., Bougamont, M., et al. (2018). Physical Conditions of Fast Glacier Flow: 1. Measurements From Boreholes Drilled to the Bed of Store Glacier, West Greenland. *Journal of Geophysical Research: Earth Surface*, *123*(2), 324–348. https://doi.org/10.1002/2017JF004529

Fausto, R. S., van As, D., Mankoff, K. D., Vandecrux, B., Citterio, M., Ahlstrøm, A. P., et al. (2021). Programme for Monitoring of the Greenland Ice Sheet (PROMICE) automatic weather station data. *Earth System Science Data*, *13*(8), 3819–3845. https://doi.org/10.5194/essd-13-3819-2021

Flowers GE, Björnsson H and Pálsson F (2003) New insights into the subglacial and periglacial hydrology of Vatnajökull, Iceland, from a distributed physical model. *Journal of Glaciology* 49(165), 257–270. doi:10.3189/172756503781830827.

Fudge, T. J., Humphrey, N. F., Harper, J. T., & Pfeffer, W. T. (2008). Diurnal fluctuations in borehole water levels: configuration of the drainage system beneath Bench Glacier, Alaska, USA. *Journal of Glaciology*, *54*(185), 297–306. https://doi.org/10.3189/002214308784886072

Gimbert, F., Tsai, V. C., Amundson, J. M., Bartholomaus, T. C., & Walter, J. I. (2016). Subseasonal changes observed in subglacial channel pressure, size, and sediment transport. *Geophysical Research Letters*, *43*(8), 3786–3794. https://doi.org/10.1002/2016GL068337

Gordon, S., Sharp, M., Hubbard, B., Smart, C., Ketterling, B., & Willis, I. (1998). Seasonal reorganization of subglacial drainage inferred from measurements in boreholes. *Hydrological Processes*, *12*(1), 105–133. https://doi.org/10.1002/(SICI)1099-1085(199801)12:1<105::AID-HYP566>3.0.CO;2-#

Gordon, S., Sharp, M., Hubbard, B., Willis, I., Smart, C., Copland, L., et al. (2001). Borehole drainage and its implications for the investigation of glacier hydrology: experiences from Haut Glacier d'Arolla, Switzerland. *Hydrological Processes*, *15*(5), 797–813. https://doi.org/10.1002/hyp.184

Harper, J., Hubbard, A., Ruskeeniemi, T., Claesson Liljedahl, L., Lehtinen, A., Booth, A., Brinkerhoff, D., Drake, H., Dow, C., Doyle, S. and Engström, J., (2011). The Greenland analogue project. Yearly report 2010 (Technical Report). Swedish Nuclear Fuel and Waste Management Co.

Hewitt I (2013) Seasonal changes in ice sheet motion due to melt water lubrication. Earth and Planetary Science Letters 371-372, 16–25. https://doi.org/10.1016/j.epsl.2013.04.022

Hoffman, M. J., Catania, G. A., Neumann, T. A., Andrews, L. C., & Rumrill, J. A. (2011). Links between acceleration, melting, and supraglacial lake drainage of the western Greenland Ice Sheet. *Journal of Geophysical Research: Earth Surface*, *116*(F4). https://doi.org/10.1029/2010JF001934

How P and others (2022) PROMICE and GC-Net automated weather station data in Greenland. GEUS Dataverse.

Hoffman, Matthew J., Andrews, L. C., Price, S. F., Catania, G. A., Neumann, T. A., Lüthi, M. P., et al. (2016). Greenland subglacial drainage evolution regulated by weakly connected regions of the bed. *Nature Communications*, *7*(1), 13903. https://doi.org/10.1038/ncomms13903

Holmlund, P. (1988). Internal Geometry and Evolution of Moulins, Storglaciären, Sweden. *Journal of Glaciology*, *34*(117), 242–248. https://doi.org/10.3189/S0022143000032305

Holmlund, P., & Hooke, R. LeB. (1983). High Water-Pressure Events in Moulins, Storglaciären, Sweden. *Geografiska Annaler. Series A, Physical Geography*, *65*(1/2), 19–25. https://doi.org/10.2307/520717

Hooke, R. L., Calla, P., Holmlund, P., Nilsson, M., & Stroeven, A. (1989). A 3 Year Record of Seasonal Variations in Surface Velocity, StorglaciÄren, Sweden. *Journal of Glaciology*, *35*(120), 235–247. https://doi.org/10.3189/S0022143000004561

Hubbard, B. P., Sharp, M. J., Willis, I. C., Nielsen, M. K., & Smart, C. C. (1995). Borehole water-level variations and the structure of the subglacial hydrological system of Haut Glacier d'Arolla, Valais, Switzerland. *Journal of Glaciology*, *41*(139), 572–583. https://doi.org/10.3189/S0022143000034894

Iken A, Röthlisberger H, Flotron A and Haeberli W (1983) The Uplift of Unteraargletscher at the Beginning of the Melt Season—A Consequence of Water Storage at the Bed? Journal of Glaciology 29(101), 28–47. doi:10.3189/S0022143000005128.

Iken, A., & Bindschadler, R. A. (1986). Combined measurements of Subglacial Water Pressure and Surface Velocity of Findelengletscher, Switzerland: Conclusions about Drainage System and Sliding Mechanism. *Journal of Glaciology*, *32*(110), 101–119. https://doi.org/10.3189/S0022143000006936

Iken, A., & Truffer, M. (1997). The relationship between subglacial water pressure and velocity of Findelengletscher, Switzerland, during its advance and retreat. *Journal of Glaciology*, *43*(144), 328–338. https://doi.org/10.3189/S0022143000003282

Jones C, Ryan J, Holt T and Hubbard A (2018) Structural glaciology of Isunguata Sermia, West Greenland. Journal of Maps 14(2), 517–527. doi:10.1080/17445647.2018.1507952.

Kamb, B. (1987). Glacier surge mechanism based on linked cavity configuration of the basal water conduit system. *Journal of Geophysical Research: Solid Earth*, *92*(B9), 9083–9100. https://doi.org/10.1029/JB092iB09p09083

King, M. (2004). Rigorous GPS data-processing strategies for glaciological applications. *Journal of Glaciology*, *50*(171), 601–607. https://doi.org/10.3189/172756504781829747

Lefeuvre, P.-M., Jackson, M., Lappegard, G., & Hagen, J. O. (2015). Interannual variability of glacier basal pressure from a 20 year record. *Annals of Glaciology*, *56*(70), 33–44. https://doi.org/10.3189/2015AoG70A019

Lefeuvre, P.-M., Zwinger, T., Jackson, M., Gagliardini, O., Lappegard, G., & Hagen, J. O. (2018). Stress Redistribution Explains Anti-correlated Subglacial Pressure Variations. *Frontiers in Earth Science*, *5*. https://doi.org/10.3389/feart.2017.00110

Lewington, E. L. M., Livingstone, S. J., Clark, C. D., Sole, A. J., & Storrar, R. D. (2020). A model for interaction between conduits and surrounding hydraulically connected distributed drainage based on geomorphological evidence from Keewatin, Canada. *The Cryosphere*, *14*(9), 2949–2976. https://doi.org/10.5194/tc-14-2949-2020

Lindbäck, K., Pettersson, R., Doyle, S. H., Helanow, C., Jansson, P., Kristensen, S. S., et al. (2014). High-resolution ice thickness and bed topography of a land-terminating section of the Greenland Ice Sheet. *Earth System Science Data*, *6*(2), 331–338. https://doi.org/10.5194/essd-6-331-2014

Livingstone, S. J., Sole, A. J., Storrar, R. D., Harrison, D., Ross, N., & Bowling, J. (2019). Brief communication: Subglacial lake drainage beneath Isunguata Sermia, West Greenland: geomorphic and ice dynamic effects. *The Cryosphere*, *13*(10), 2789–2796. https://doi.org/10.5194/tc-13-2789-2019

Lüthi, M., Funk, M., Iken, A., Gogineni, S., & Truffer, M. (2002). Mechanisms of fast flow in Jakobshavn Isbræ, West Greenland: Part III. Measurements of ice deformation, temperature and cross-borehole conductivity in boreholes to the bedrock. *Journal of Glaciology*, *48*(162), 369–385. https://doi.org/10.3189/172756502781831322

Luthi, M. (2013) Gauging Greenland's Subglacial Water, *Science,* 341 (6147), 721-722, https://doi.org/10.1126/science.1242672

Ng F (2000) Canals under sediment-based ice sheets. Annals of Glaciology, 30 (1), 146–152. http://doi.org/10.3189/172756400781820633

Maier, N., Humphrey, N., Harper, J., & Meierbachtol, T. (2019). Sliding dominates slow-flowing margin regions, Greenland Ice Sheet. Science Advances, 5(7), eaaw5406. https://doi.org/10.1126/sciadv.aaw5406

Mair, D., Nienow, P., Willis, I., & Sharp, M. (2001). Spatial patterns of glacier motion during a high-velocity event: Haut Glacier d'Arolla, Switzerland. *Journal of Glaciology*, *47*(156), 9–20. https://doi.org/10.3189/172756501781832412

751 Mankoff, K. D., Noël, B., Fettweis, X., Ahlstrøm, A. P., Colgan, W., Kondo, K., et al. (2020).
752 Greenland liquid water discharge from 1958 through 2019. *Earth System Science Data*,
753 *12*(4), 2811–2841. https://doi.org/10.5194/essd-12-2811-2020

754 Meierbachtol, T., Harper, J., & Humphrey, N. (2013). Basal Drainage System Response to
755 Increasing Surface Melt on the Greenland Ice Sheet. *Science*, *341*(6147), 777–779.
756 https://doi.org/10.1126/science.1235905

757 Mejia, J. Z., Gulley, J. D., Trunz, C., Covington, M. D., Bartholomaus, T. C., Xie, S., & Dixon, T.
758 H. (2021). Isolated Cavities Dominate Greenland Ice Sheet Dynamic Response to Lake
759 Drainage. *Geophysical Research Letters*, *48*(19), e2021GL094762.
760 https://doi.org/10.1029/2021GL094762

761 Mejia, J. Z., Gulley, J. D., Trunz, C., Covington, M. D., Bartholomaus, T. C., Breithaupt, C., et
762 al. (2022). Moulin Density Controls the Timing of Peak Pressurization Within the
763 Greenland Ice Sheet's Subglacial Drainage System. *Geophysical Research Letters*,
764 *49*(22), e2022GL100058. https://doi.org/10.1029/2022GL100058

765 Morlighem, M., Williams, C. N., Rignot, E., An, L., Arndt, J. E., Bamber, J. L., et al. (2017).
766 BedMachine v3: Complete Bed Topography and Ocean Bathymetry Mapping of
767 Greenland From Multibeam Echo Sounding Combined With Mass Conservation.
768 *Geophysical Research Letters*, *44*(21), 11,051-11,061.
769 https://doi.org/10.1002/2017GL074954

770 Morlighem, Mathieu & Et Al. (2022). IceBridge BedMachine Greenland, Version 5. NASA
771 National Snow and Ice Data Center Distributed Active Archive Center.
772 https://doi.org/10.5067/GMEVBWFLWA7X

773 Muñoz-Sabater, J., Dutra, E., Agustí-Panareda, A., Albergel, C., Arduini, G., Balsamo, G., et
774 al. (2021). ERA5-Land: a state-of-the-art global reanalysis dataset for land applications.
775 *Earth System Science Data*, *13*(9), 4349–4383. https://doi.org/10.5194/essd-13-4349-
776 2021

777 Murray, T., & Clarke, G. K. C. (1995). Black-box modeling of the subglacial water system.
778 *Journal of Geophysical Research: Solid Earth*, *100*(B6), 10231–10245.
779 https://doi.org/10.1029/95JB00671

780 Nanni, U., Gimbert, F., Vincent, C., Gräff, D., Walter, F., Piard, L., & Moreau, L. (2020).
781 Quantification of seasonal and diurnal dynamics of subglacial channels using seismic
782 observations on an Alpine glacier. *The Cryosphere*, *14*(5), 1475–1496.
783 https://doi.org/10.5194/tc-14-1475-2020

784 Nienow, P. W., Hubbard, A. L., Hubbard, B. P., Chandler, D. M., Mair, D. W. F., Sharp, M. J.,
785 & Willis, I. C. (2005). Hydrological controls on diurnal ice flow variability in valley

786 glaciers. *Journal of Geophysical Research: Earth Surface*, *110*(F4).
787 https://doi.org/10.1029/2003JF000112

788 Nye, J. F. (1976). Water Flow in Glaciers: Jökulhlaups, Tunnels and Veins. *Journal of*
789 *Glaciology*, *17*(76), 181–207. https://doi.org/10.3189/S002214300001354X

790 Pitcher, L. H., Smith, L. C., Gleason, C. J., Miège, C., Ryan, J. C., Hagedorn, B., et al. (2020).
791 Direct Observation of Winter Meltwater Drainage From the Greenland Ice Sheet.
792 *Geophysical Research Letters*, *47*(9), e2019GL086521.
793 https://doi.org/10.1029/2019GL086521

794 Prior-Jones, M. R., Bagshaw, E. A., Lees, J., Clare, L., Burrow, S., Werder, M. A., et al. (2021).
795 Cryoegg: development and field trials of a wireless subglacial probe for deep, fast-
796 moving ice. *Journal of Glaciology*, *67*(264), 627–640.
797 https://doi.org/10.1017/jog.2021.16

798 Rada, C., & Schoof, C. (2018). Channelized, distributed, and disconnected: subglacial
799 drainage under a valley glacier in the Yukon. *The Cryosphere*, *12*(8), 2609–2636.
800 https://doi.org/10.5194/tc-12-2609-2018

801 Rada Giacaman, C. A., & Schoof, C. (2023). Channelized, distributed, and disconnected:
802 spatial structure and temporal evolution of the subglacial drainage under a valley
803 glacier in the Yukon. *The Cryosphere*, *17*(2), 761–787. https://doi.org/10.5194/tc-17-
804 761-2023

805 Röthlisberger, H. (1972). Water Pressure in Intra- and Subglacial Channels. *Journal of*
806 *Glaciology*, *11*(62), 177–203. https://doi.org/10.3189/S0022143000022188

807 Ryser, C., Lüthi, M. P., Andrews, L. C., Hoffman, M. J., Catania, G. A., Hawley, R. L., et al.
808 (2014). Sustained high basal motion of the Greenland ice sheet revealed by borehole
809 deformation. *Journal of Glaciology*, *60*(222), 647–660.
810 https://doi.org/10.3189/2014JoG13J196

811 Sauter, T., Arndt, A., & Schneider, C. (2020). COSIPY v1.3 – an open-source coupled
812 snowpack and ice surface energy and mass balance model. *Geoscientific Model*
813 *Development*, *13*(11), 5645–5662. https://doi.org/10.5194/gmd-13-5645-2020

814 Schoof, C. (2010). Ice-sheet acceleration driven by melt supply variability. *Nature*,
815 *468*(7325), 803–806. https://doi.org/10.1038/nature09618

816 Shepherd, A., Hubbard, A., Nienow, P., King, M., McMillan, M., & Joughin, I. (2009).
817 Greenland ice sheet motion coupled with daily melting in late summer. *Geophysical*
818 *Research Letters*, *36*(1). https://doi.org/10.1029/2008GL035758

819 Sole, A., Nienow, P., Bartholomew, I., Mair, D., Cowton, T., Tedstone, A., & King, M. A.
820 (2013). Winter motion mediates dynamic response of the Greenland Ice Sheet to

warmer summers. *Geophysical Research Letters*, *40*(15), 3940–3944. https://doi.org/10.1002/grl.50764

Stone, D. B., & Clarke, G. K. C. (1996). In Situ Measurements of Basal Water Quality and Pressure as an Indicator of the Character of Subglacial Drainage Systems. *Hydrological Processes*, *10*(4), 615–628. https://doi.org/10.1002/(SICI)1099-1085(199604)10:4<615::AID-HYP395>3.0.CO;2-M

Sugiyama, S., Bauder, A., Huss, M., Riesen, P., & Funk, M. (2008). Triggering and drainage mechanisms of the 2004 glacier-dammed lake outburst in Gornergletscher, Switzerland. *Journal of Geophysical Research: Earth Surface*, *113*(F4). https://doi.org/10.1029/2007JF000920

Tedstone, A. J., Nienow, P. W., Gourmelen, N., & Sole, A. J. (2014). Greenland ice sheet annual motion insensitive to spatial variations in subglacial hydraulic structure. *Geophysical Research Letters*, *41*(24), 8910–8917. https://doi.org/10.1002/2014GL062386

Tranter, M., Sharp, M. J., Brown, G. H., Willis, I. C., Hubbard, B. P., Nielsen, M. K., et al. (1997). Variability in the Chemical Composition of in Situ Subglacial Meltwaters. *Hydrological Processes*, *11*(1), 59–77. https://doi.org/10.1002/(SICI)1099-1085(199701)11:1<59::AID-HYP403>3.0.CO;2-S

van de Wal, R. S. W., Boot, W., van den Broeke, M. R., Smeets, C. J. P. P., Reijmer, C. H., Donker, J. J. A., & Oerlemans, J. (2008). Large and Rapid Melt-Induced Velocity Changes in the Ablation Zone of the Greenland Ice Sheet. *Science*, *321*(5885), 111–113. https://doi.org/10.1126/science.1158540

van de Wal, R. S. W., Smeets, C. J. P. P., Boot, W., Stoffelen, M., van Kampen, R., Doyle, S. H., et al. (2015). Self-regulation of ice flow varies across the ablation area in south-west Greenland. *The Cryosphere*, *9*(2), 603–611. https://doi.org/10.5194/tc-9-603-2015

Welch, P. (1967). The use of fast Fourier transform for the estimation of power spectra: A method based on time averaging over short, modified periodograms. *IEEE Transactions on Audio and Electroacoustics*, *15*(2), 70–73. https://doi.org/10.1109/TAU.1967.1161901

Werder, M. A., Hewitt, I. J., Schoof, C. G., & Flowers, G. E. (2013). Modeling channelized and distributed subglacial drainage in two dimensions. *Journal of Geophysical Research: Earth Surface*, *118*(4), 2140–2158. https://doi.org/10.1002/jgrf.20146

Weertman, J. (1972). General theory of water flow at the base of a glacier or ice sheet. *Reviews of Geophysics*, *10*(1), 287–333. https://doi.org/10.1029/RG010i001p00287

Wright, P. J., Harper, J. T., Humphrey, N. F., & Meierbachtol, T. W. (2016). Measured basal water pressure variability of the western Greenland Ice Sheet: Implications for hydraulic potential. *Journal of Geophysical Research: Earth Surface*, *121*(6), 1134–1147. https://doi.org/10.1002/2016JF003819

References from the Supporting Information

Fausto, R. S., van As, D., Mankoff, K. D., Vandecrux, B., Citterio, M., Ahlstrøm, A. P., et al. (2021). Programme for Monitoring of the Greenland Ice Sheet (PROMICE) automatic weather station data. *Earth System Science Data*, *13*(8), 3819–3845. https://doi.org/10.5194/essd-13-3819-2021

How P and others (2022) PROMICE and GC-Net automated weather station data in Greenland. GEUS Dataverse.

Mankoff, K. D., Noël, B., Fettweis, X., Ahlstrøm, A. P., Colgan, W., Kondo, K., et al. (2020). Greenland liquid water discharge from 1958 through 2019. Earth System Science Data, 12(4), 2811–2841. https://doi.org/10.5194/essd-12-2811-2020

Porter, C., Howat, I., Noh, M.J., Husby, E., Khuvis, S., Danish, E., Tomko, K., Gardiner, J., Negrete, A., Yadav, B., Klassen, J., Kelleher, C., Cloutier, M., Bakker, J., Enos, J., Arnold, G., Bauer, G., and Morin, P., 2023, "ArcticDEM – Strips, Version 4.1", https://doi.org/10.7910/DVN/3VDC4W, Harvard Dataverse, V1, [3rd March 2025].

Supporting Information

Introduction. The supporting information includes photographs of the cryoegg field deployment, alongside detailed methods for sensor calibration and the calculation of hydraulic head as a percentage of ice overburden. Additionally, it presents supplementary figures for points discussed in the main text.

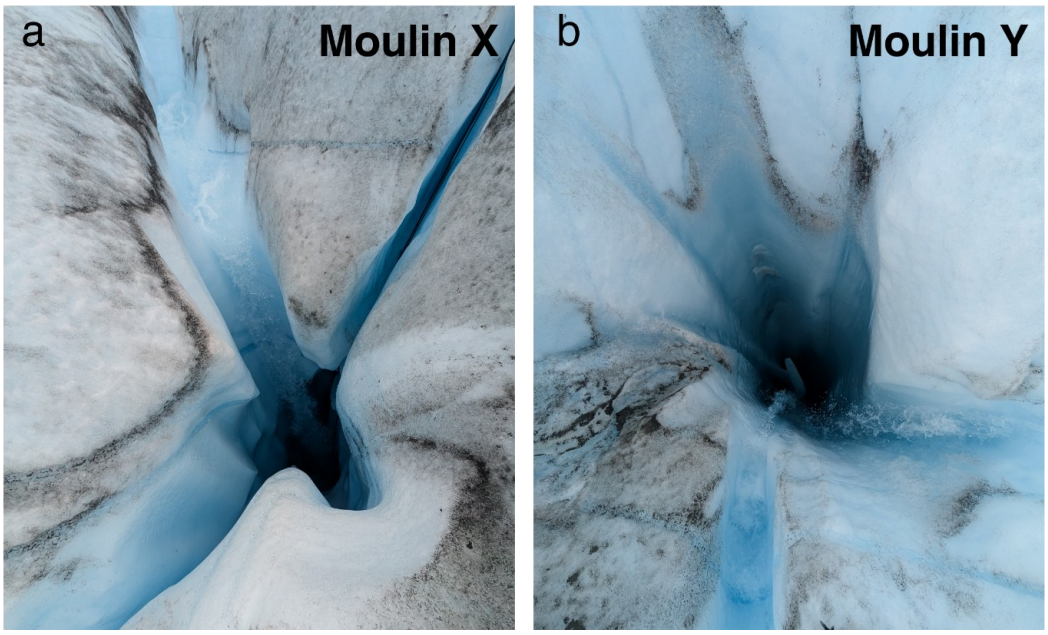

Figure S1. a) Moulin X on 26th July 2024. b) Moulin Y on 26th July 2024.

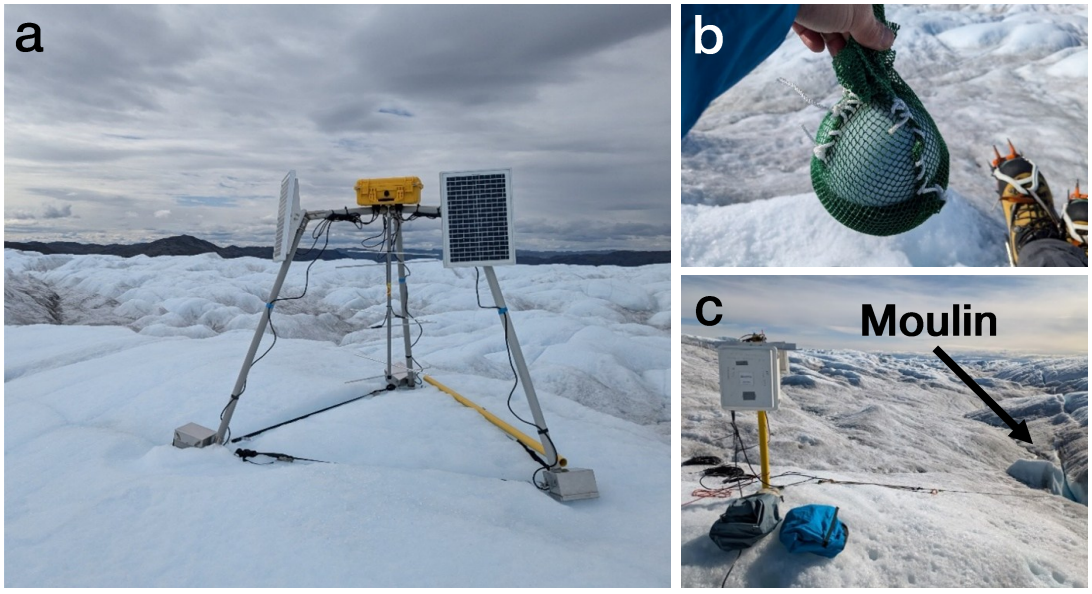

Figure S2. a) Cryoegg receiver station with Iridium uplink. b) Deployed Cryoegg Y1 with foam and mesh floatation device. c) Moulin X site with Campbell logger for Geokon.

Text S1.

1. Calibration of Geokon piezometer

The pressure value measured by the Geokon 4500 vibrating wire piezometer was corrected for variations in atmospheric pressure using the PROMICE automated weather stations (Fausto et al., 2021, How et al, 2022). The time-varying component of atmospheric pressure observed at three nearby automated weather stations (KAN_B - 5.6 km, KAN_T - 5.6 km, KAN_L - 12 km) agrees well with the variations in atmospheric pressure observed at the Cryoegg receiver (R2=0.994 to 0.996, p<0.001). The upper boom atmospheric pressure at 2024-07-09 18:55:300 UTC for each of the PROMICE weather stations is subtracted from the hourly time series and the average time-varying change in atmospheric pressure is calculated. This change in pressure is then subtracted from the pressure recorded by the Geokon 4500 piezometer, which was calibrated to atmospheric pressure at the same timestamp, so that changes in atmospheric pressure are compensated prior to interpretation as hydraulic head in meters.

2. Cryoegg sensor deployment and calibration

Upon deployment, the time taken for Cryoegg Y1 to free-fall from the ice surface to a ledge inside the moulin (causing an audible thud) was measured (Movie S1). The measured fall time was 3.75 s. Using Equation (S1), the depth of Cryoegg Y1 was estimated to be approximately 69 m below the ice surface.

$$h = \frac{1}{2} g t^2 \text{ (Equation S1)}$$

Initial electrical conductivity and water pressure readings confirmed the sensor was positioned above the moulin's current water level. Due to the minimal deviation in hydraulic head between all the sensors in Moulin X and Y after calibration, we are also confident that Cryoegg Y1 did not move from this ice ledge.

Each Cryoegg was individually calibrated, to account for small variations in sensor geometry. The EC sensors were calibrated using NaCl solutions of varying conductivity, and the pressure sensor was zeroed using a unique initial offset between the TE pressure sensor in the surface receiver and the Keller sensor in each egg.

The ice thickness at each moulin was estimated from interpolated ground penetrating radar lines close to our site. For Moulin X the ice thickness was 446 m, and 450 m for Moulin Y. To provide an approximate estimate of orthometric ice surface elevation we use the ArcticDEM mosaic version 4.1 (Porter at al., 2023). From this, the bed elevation below each moulin was estimated to be approximately 50 m. This places Cryoegg Y1 at 381 m above the bed (ice thickness – sensor depth below surface) and at an orthometric height (Z_{sensor}) of 433 m a.s.l.

From the time series of uncalibrated water depth above each sensor, we select a time when diurnal oscillations suggest a well-connected system, with the variations of each

moulin in phase (e.g., 5th August 2024 at 21:00 UTC; Fig. S3) when all sensors are under water. During this time, we assume that the two moulins are well connected and in hydraulic equilibrium, with negligible friction loss between them (Röthlisberger 1972; Shreve 1972). This assumption is further justified by the moulins' close proximity (~100 m apart) and their similar estimated ice thicknesses.

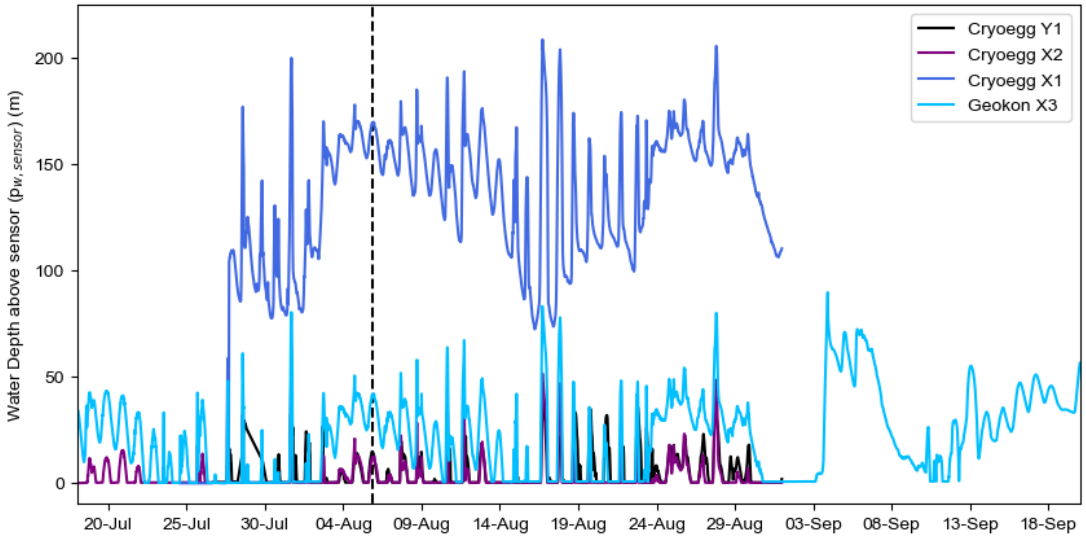

Figure S3. Time series of the water depth above each sensor in Moulin X and Moulin Y. Dashed black line shows the chosen calibration date of 5th August 2024 at 21:00 UTC.

Calibration to orthometric hydraulic head

For the 5th August 2024 at 21:00 UTC Cryoegg Y1 measured a water depth above the sensor ($p_{w,sensor}$) of 14 m. This equates to a water depth in the moulin ($p_{w,moulin}$) of 395 m and an orthometric height above sea level (Z_w) of 447 m a.s.l. (Equation S2).

$$Z_w = p_{w,sensor} + Z_{sensor} \text{ (Equation S2)}$$

Assuming hydraulic equilibrium between the two moulins, the orthometric height of the other sensors can be calculated using Equation S3.

$$Z_{sensor} = (p_{w,moulin} - p_{w,sensor}) + Z_b \text{ (Equation S3)}$$

Where Z_b is the orthometric bed elevation. This gives an orthometric height of the other sensors at 279 m a.s.l for Cryoegg X1, 437 m a.s.l. for Cryoegg X2 and 407 m a.s.l. for Geokon X3.

Calibration to percentage of ice overburden

To calculate water pressure in each moulin as a percentage of ice-overburden pressure we use Equation S4 and Equation S5.

$$p_i = \rho_i g H cos(\beta) \text{ (Equation S4)}$$

$$p_w = \rho_w g p_{w,moulin} \text{ (Equation S5)}$$

Where ρ_i is 910 kg m^{-3}, ρ_i is 999.8 kg m^{-3}, β is the bed slope and H is the ice thickness at each moulin.

Table S1: Discharge measurements for the supraglacial stream feeding Moulin X in July 2024 determined using salt tracing. Conductivity curves from the salt trace were recorded by a submerged Keller logger to calculate flow rates.

Date (UTC)	Stream Discharge (m^3s^{-1})
15/07/2024 17:00	0.050
18/07/2024 14:00	0.034
18/07/2024 15:00	0.057

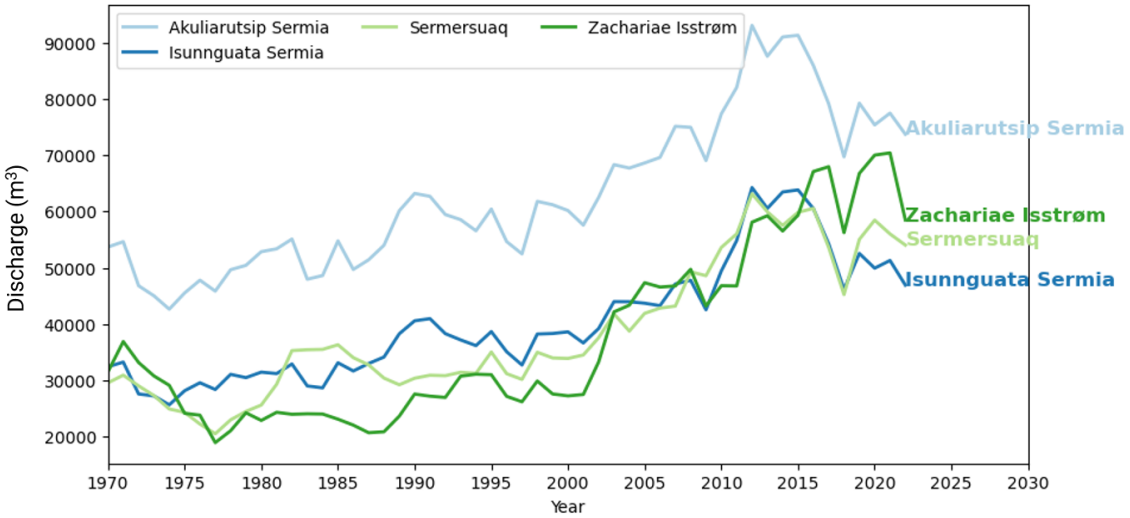

Figure S4: The total annual runoff (6-year rolling mean) of the top four largest outlets. Data is from Mankoff et al., (2022), with the runoff derived from RACMO.

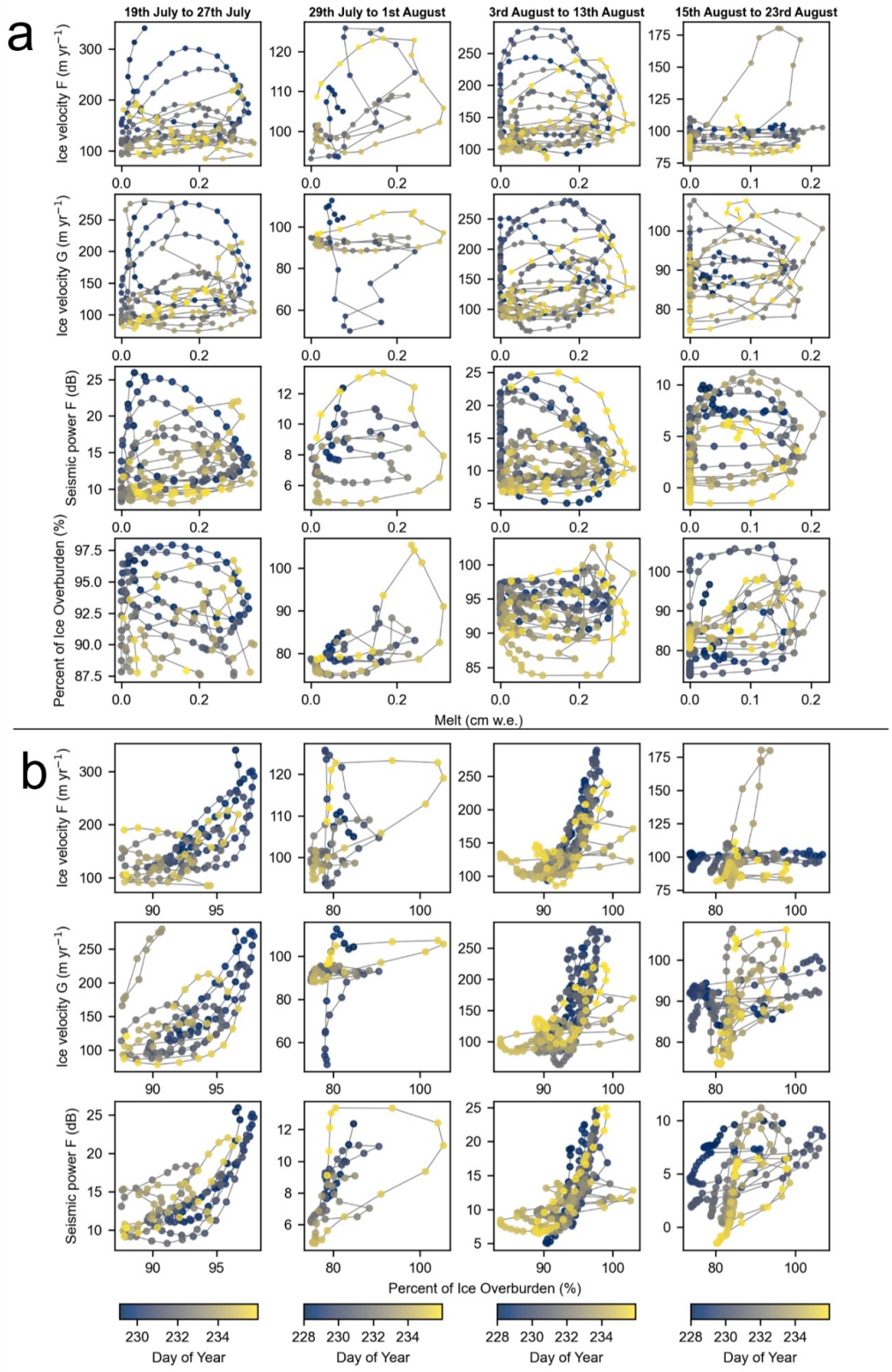

Figure S5: a) Hysteresis plots between hourly surface melt and all other variables (ice velocity at F and G, seismic tremor and median moulin hydraulic head of all sensors). b) Hysteresis plots between median moulin hydraulic head and ice velocity at F and G, and seismic tremor. Colours denote the day of year in 2024.

Movie S1. Video showing the deployment of Cryoegg Y1 down Moulin Y on the 18th July 2024.